

# *Relationship of tropospheric stability to climate sensitivity and Earth's observed radiation budget*

Article

Accepted Version

Ceppi, P. and Gregory, J. M. (2017) Relationship of tropospheric stability to climate sensitivity and Earth's observed radiation budget. *Proceedings of the National Academy of Sciences of the United States of America*, 114 (50). pp. 13126-13131. ISSN 0027-8424 doi: <https://doi.org/10.1073/pnas.1714308114> Available at <http://centaur.reading.ac.uk/74155/>

It is advisable to refer to the publisher's version if you intend to cite from the work.

Published version at: <http://dx.doi.org/10.1073/pnas.1714308114>

To link to this article DOI: <http://dx.doi.org/10.1073/pnas.1714308114>

Publisher: National Academy of Sciences

All outputs in CentAUR are protected by Intellectual Property Rights law, including copyright law. Copyright and IPR is retained by the creators or other copyright holders. Terms and conditions for use of this material are defined in the [End User Agreement](#).

[www.reading.ac.uk/centaur](http://www.reading.ac.uk/centaur)

## **CentAUR**

Central Archive at the University of Reading

Reading's research outputs online

# Relationship of tropospheric stability to climate sensitivity and Earth's observed radiation budget

Paulo Ceppi<sup>a,1</sup> and Jonathan M. Gregory<sup>b,c</sup>

<sup>a</sup>Department of Meteorology, University of Reading, Reading RG6 6BB, United Kingdom; <sup>b</sup>NCAS-Climate, University of Reading, Reading RG6 6BB, United Kingdom; <sup>c</sup>Met Office Hadley Centre, Exeter EX1 3PB, United Kingdom

This manuscript was compiled on November 3, 2017

**Climate feedbacks generally become smaller in magnitude over time under CO<sub>2</sub> forcing in coupled climate models, leading to an increase in the effective climate sensitivity, the estimated global-mean surface warming in steady state for doubled CO<sub>2</sub>. Here we show that the evolution of climate feedbacks in models is consistent with the effect of a change in tropospheric stability, as has recently been hypothesized, and the latter is itself driven by the evolution of the pattern of sea surface temperature response. The change in climate feedback is mainly associated with a decrease in marine tropical low cloud (a more positive shortwave cloud feedback) and with a less negative lapse rate feedback, as expected from a decrease in stability. Smaller changes in surface albedo and humidity feedbacks also contribute to the overall change in feedback, but are unexplained by stability. The spatial pattern of feedback changes closely matches the pattern of stability changes, with the largest increase in feedback occurring in the tropical East Pacific. Relationships qualitatively similar to those in the models among sea surface temperature pattern, stability, and radiative budget are also found in observations on interannual time scales. Our results suggest that constraining the future evolution of sea surface temperature patterns and tropospheric stability will be necessary for constraining climate sensitivity.**

climate sensitivity | climate feedbacks | clouds | satellite observations

How much Earth will warm in response to future greenhouse gas emissions is a fundamental question in climate science. Accordingly, a widely-used metric for the evaluation and comparison of climate models is the equilibrium climate sensitivity (ECS), the steady-state global-mean surface temperature change for a doubling of CO<sub>2</sub> concentration relative to the pre-industrial state. A common method to estimate ECS involves assuming the climate system response to a radiative forcing  $F$  to be proportional to global-mean temperature  $T$ , according to  $\lambda = (N - F)/T$  where  $\lambda < 0$  (1). Here  $N$  denotes the net downward radiative imbalance,  $N - F$  is the radiative response, and  $\lambda$  is the proportionality constant between radiative response and global-mean warming. Because its value depends on climate feedback processes involving changes in the atmospheric lapse rate, water vapor concentration, cloud properties, and surface albedo with warming, the proportionality constant  $\lambda$  is usually referred to as the climate feedback parameter. Assuming  $\lambda$  stays constant in time, we may estimate ECS by extrapolating the relationship between  $N - F$  and  $T$  to the temperature at which  $N = 0$ , i.e. radiative balance is restored:  $ECS = -F/\lambda$ , if  $F$  represents the forcing of a doubling of CO<sub>2</sub>.

Although convenient, the assumption of a constant proportionality factor  $\lambda$  between radiative response and global-mean warming does not hold perfectly in climate models. Indeed, in most climate models  $\lambda$  decreases in magnitude as time passes following an increase in CO<sub>2</sub> concentration, leading

to an increase in the “effective” climate sensitivity over time (2–13). However, the mechanisms of this evolution are currently not understood. Targeted climate model experiments have pointed to the role of evolving patterns of sea surface temperature (SST) increase in driving the evolution of climate sensitivity and feedbacks (9, 14–17), which may alternatively also be interpreted as changing patterns of ocean heat uptake (5, 18–20). Two distinct hypotheses have been proposed to link the evolution of SSTs to climate feedbacks over the course of the transient response to CO<sub>2</sub> forcing:

1. Feedbacks are assumed to scale linearly with local temperature, but are fixed in time. Global-mean feedback varies only as a result of evolving surface warming patterns, causing the spatial weighting of local feedbacks to change as time passes (7).
2. The SST evolution favors a decrease in tropospheric stability, resulting in less free-tropospheric warming per unit surface warming. This stability decrease reduces the ability of the atmosphere to cool radiatively to space from the upper troposphere (a less negative lapse rate feedback; 17), and acts to decrease low cloud cover in subsidence regions, enhancing the absorption of solar radiation (a more positive cloud feedback; 15–17). Under this hypothesis, feedbacks may vary locally in time.

Here we show that the evolution of climate feedbacks during the transient response to increased CO<sub>2</sub> in current coupled climate models is consistent with the effects of changes in

## Significance Statement

In current climate models, the anticipated amount of warming under greenhouse gas forcing, quantified by the “effective climate sensitivity”, increases as time passes. Consequently, effective climate sensitivity values inferred from the historical record may underestimate the future warming. However, the mechanisms of this increase in effective climate sensitivity are not understood, limiting our confidence in climate model projections of future climate change. Here we present observational and modeling evidence that the magnitude of effective climate sensitivity partly depends on the evolution of the vertical profile of atmospheric warming. In climate models, as the Earth warms overall, the warming becomes increasingly muted aloft, and this alters the strength of feedbacks controlling the radiative response to greenhouse gas forcing.

P.C. designed research and analyzed the data. P.C. and J.M.G. jointly wrote the paper.

The authors declare no conflict of interest.

<sup>1</sup>To whom correspondence should be addressed. E-mail: p.ceppi@reading.ac.uk

125  
126  
127  
128  
129  
130  
131  
132  
133  
134  
135  
136  
137  
138  
139  
140  
141  
142  
143  
144  
145  
146  
147  
148  
149  
150  
151  
152  
153  
154  
155  
156  
157  
158  
159  
160  
161  
162  
163  
164  
165  
166  
167  
168  
169  
170  
171  
172  
173  
174  
175  
176  
177  
178  
179  
180  
181  
182  
183  
184  
185  
186

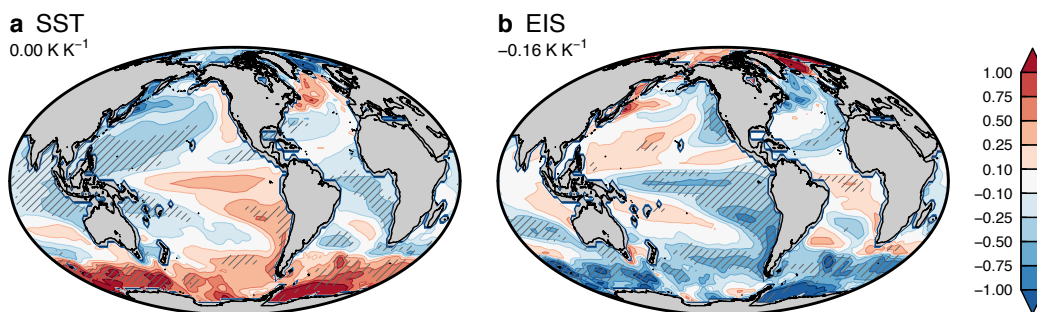


**Fig. 1.** Multi-model mean difference in patterns of (a) SST and (b) EIS change. The patterns of change are first calculated separately for each model for the early (years 1–20) and late (21–150) periods by regressing local annual-mean SST or EIS against global-mean annual-mean surface temperature; then the difference is calculated as late minus early period. The patterns of change in the early and late periods are shown in Fig. S1. Numbers in the top left corner of each panel denote global-mean values. Hatching denotes a multi-model mean absolute anomaly larger than one standard deviation across models.

143 tropospheric stability, following hypothesis 2 above. Furthermore, we demonstrate that observed interannual relationships between SST pattern, tropospheric stability, and the radiative budget qualitatively support the relationships found in climate models. Our results therefore suggest that constraining climate sensitivity will require constraints on the long-term evolution of SST and tropospheric stability.

## 151 Results

### 153 Changes in the evolution of SST and tropospheric stability.

154 We first consider the SST evolution during the first 150 years following a quadrupling of CO<sub>2</sub> concentration in a set of 15 coupled climate models (Materials and Methods; Table S1). The changes over the course of the simulations are defined as the difference in responses between years 1–20 (hereafter “early period”) and years 21–150 (“late period”). As the planet warms, the pattern of SST response per unit global warming evolves towards enhanced warming in the tropical East Pacific, in the Southern Ocean, in the North Atlantic, and to a lesser extent in the Northeast Pacific, while the tropical West Pacific, Northwest Pacific, tropical Atlantic, and much of the Indian Ocean experience reduced warming relative to the global average (Fig. 1a). The global-mean difference between patterns of SST change is very close to zero. (The global-mean difference between patterns of surface temperature change, including land areas, would be exactly zero by construction.) The overall spatial structure of the SST evolution is reasonably robust among models (hatching in Fig. 1a). The characteristics of the SST evolution are also similar to those found in previous studies using different sets of climate models (7, 9, 21). The delayed warming in the East Pacific and in the Southern Ocean is broadly consistent with the effects of upwelling (22, 23), but additional coupled ocean-atmosphere processes likely contribute to the evolution of the SST pattern (22, 24).

179 We now provide evidence that the evolution of the SST warming pattern favors a decrease in tropospheric stability. As a stability metric, we use the estimated inversion strength (EIS; 25), a measure of the strength of the inversion at the top of the boundary layer based on the difference in potential temperature between the surface and 700 hPa. EIS accounts for the temperature dependence of the moist adiabat to quantify the effective stability of the lower troposphere, and is tradition-

205 ally defined over ocean regions only. In observations, EIS is strongly correlated with marine low cloud cover in subsidence regions (25), consistent with the notion that a stronger inversion is more effective at trapping moisture in the boundary layer.

210 How do we expect the SST pattern to affect tropospheric stability? At any point in space, the stability change depends on the relative change in surface and free-tropospheric temperature. In the tropics, free-tropospheric temperature is largely set by the evolution of SST in warm, convective regions, such as the West Pacific warm pool, where the lapse rate is pegged to a moist adiabat owing to moist convection (26, 27). This constraint implies that the warmest regions should always remain nearly neutrally stable. Away from warm convective regions, however, the stability response will roughly depend on the ratio of local SST change to SST change in the warm pool (15). If local SST increases more than in the warm pool, stability will decrease because the free-tropospheric temperature will increase less than predicted by a local moist adiabat; the opposite would be true if local SST increased less than in the warm pool. While strictly speaking the constraint on free-tropospheric temperature applies to the tropics only, extratropical free-tropospheric temperature should be influenced by SST changes in warmer convective regions, so that a similar argument can be applied to qualitatively interpret extratropical stability changes. Although we argue that the SST pattern is the main control on the time evolution of tropospheric stability in our model simulations, additional processes can also affect stability as quantified by EIS – for example land-sea temperature contrasts and CO<sub>2</sub> concentrations (28).

235 The differences in stability response between the early and late periods in Fig. 1b are consistent with the above reasoning. The EIS difference in the warm pool around the Maritime Continent is small. Because the warm pool is warming less than average, the EIS response becomes more negative in most other regions; the larger the relative warming, the larger the stability decrease. This yields a global-mean decrease in the response of tropospheric stability to warming. It is noteworthy that the global-mean EIS response becomes more negative as time passes in all models included in this analysis (Fig. S2a).

247 **Changes in climate feedbacks.** We will now show that the evolution of climate feedbacks is consistent with the changes in

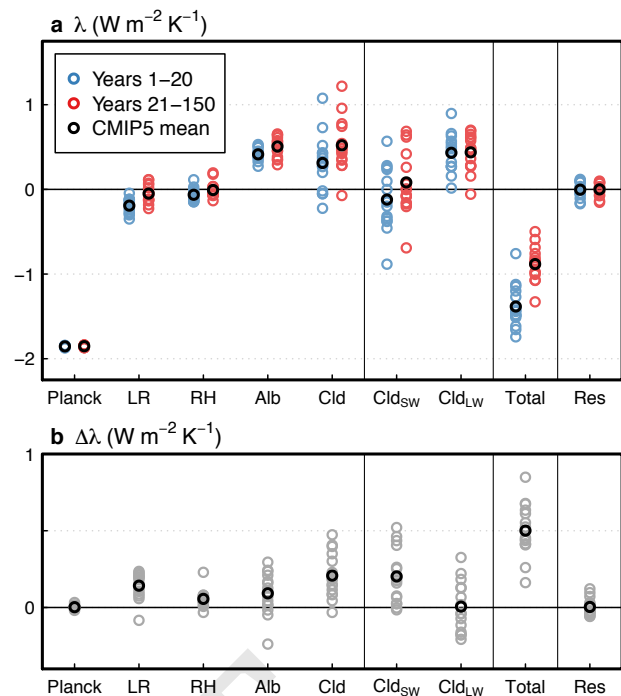
187  
188  
189  
190  
191  
192  
193  
194  
195  
196  
197  
198  
199  
200  
201  
202  
203  
204  
205  
206  
207  
208  
209  
210  
211  
212  
213  
214  
215  
216  
217  
218  
219  
220  
221  
222  
223  
224  
225  
226  
227  
228  
229  
230  
231  
232  
233  
234  
235  
236  
237  
238  
239  
240  
241  
242  
243  
244  
245  
246  
247  
248

249 tropospheric stability over the course of the transient response  
 250 to CO<sub>2</sub> forcing. Figure 2 shows the changes in global-mean  
 251 feedback parameter decomposed into the contributions of tem-  
 252 perature, water vapor, surface albedo, and clouds (using radiative  
 253 kernels; Materials and Methods). On average, the total  
 254 feedback increases by 0.50 W m<sup>-2</sup> K<sup>-1</sup> (-1.38 to -0.88 W  
 255 m<sup>-2</sup> K<sup>-1</sup>), consistent with previous findings (9). Consequently,  
 256 the estimated ECS increases by 0.57 K on average (2.83 to  
 257 3.40 K; Fig. S2b). The change in feedback is primarily due to  
 258 the effect of clouds (0.21 W m<sup>-2</sup> K<sup>-1</sup>), followed by the lapse  
 259 rate feedback (0.14 W m<sup>-2</sup> K<sup>-1</sup>), with smaller contributions  
 260 of changes in surface albedo (0.09 W m<sup>-2</sup> K<sup>-1</sup>) and relative  
 261 humidity (0.06 W m<sup>-2</sup> K<sup>-1</sup>). The increase in cloud feedback  
 262 is almost entirely due to a change in shortwave reflection (0.20  
 263 W m<sup>-2</sup> K<sup>-1</sup>). Since the mean residual is near zero, it does  
 264 not contribute to the change in total feedback parameter.

265 The results in Fig. 2 are thus consistent with the expected  
 266 effect of a stability decrease following hypothesis 2: a decrease  
 267 in low cloud amount (causing a more positive shortwave cloud  
 268 feedback), and a less negative lapse rate feedback, these two  
 269 effects jointly accounting for most of the increase in feedback  
 270 parameter and climate sensitivity. While changes in factors  
 271 other than stability – particularly local SST, subsidence, and  
 272 free-tropospheric humidity – may also affect the evolution  
 273 of the cloud response to global warming (29, 30), previous  
 274 evidence from climate model experiments suggests that the  
 275 stability effect dominates the cloud response to evolving tropi-  
 276 cal SST patterns (15). In further support for this conclusion,  
 277 the relationship between tropospheric stability and feedbacks  
 278 broadly holds across models: a larger stability decrease is as-  
 279 sociated with a larger increase in feedback parameter (Fig. S3,  
 280 Text S1–S2). Stability changes account for less than half  
 281 of the inter-model spread in net feedback changes, however  
 282 ( $r^2 = 0.40$ , Fig. S3a), indicating that effects other than stabil-  
 283 ity must also contribute to this spread (Text S2).

284 The joint effect of cloud and lapse rate feedbacks accounts  
 285 for about 70% of the change in net feedback in our set of mod-  
 286 els, leaving part of the change unexplained. We have calculated  
 287 how much of the evolution in global feedback parameter can  
 288 be ascribed to a change in spatial weighting of local feed-  
 289 backs as the warming pattern evolves, following hypothesis  
 290 1 (Fig. S4). The result suggests that the increases in surface  
 291 albedo and relative humidity feedbacks are in part associated  
 292 with the evolution of the warming pattern (0.05 and 0.04 W  
 293 m<sup>-2</sup> K<sup>-1</sup> respectively; Text S3). While the increase in sur-  
 294 face albedo feedback is consistent with the evolution towards  
 295 enhanced high-latitude warming (Text S3; 7), the mechanisms  
 296 of change in global relative humidity feedback (via either of  
 297 the hypotheses or alternative mechanisms) remain unknown.

298 The linkage between climate feedbacks and tropospheric  
 299 stability is particularly striking when considering the spatial  
 300 distribution of the changes. Generally speaking, the feedbacks  
 301 become more positive in regions where the EIS response de-  
 302 creases (compare Figs. 1b and 3), and vice-versa. The largest  
 303 increase in feedback parameter occurs in the tropical Central  
 304 and East Pacific, where the EIS response becomes substan-  
 305 tially more negative as the planet warms. Although the EIS  
 306 change over the Southern Ocean is comparable or larger in  
 307 magnitude, the local change in cloud feedback is generally  
 308 small; this may be because processes unrelated to tropospheric  
 309 stability dominate the cloud response to warming at high  
 310



311  
312  
313  
314  
315  
316  
317  
318  
319  
320  
321  
322  
323  
324  
325  
326  
327  
328  
329  
330  
331  
332  
333  
334  
335  
336  
337  
338  
339  
340  
341  
342  
343  
344  
345  
346  
347  
348  
349  
350  
351  
352  
353  
354  
355  
356  
357  
358  
359  
360  
361  
362  
363  
364  
365  
366  
367  
368  
369  
370  
371  
372

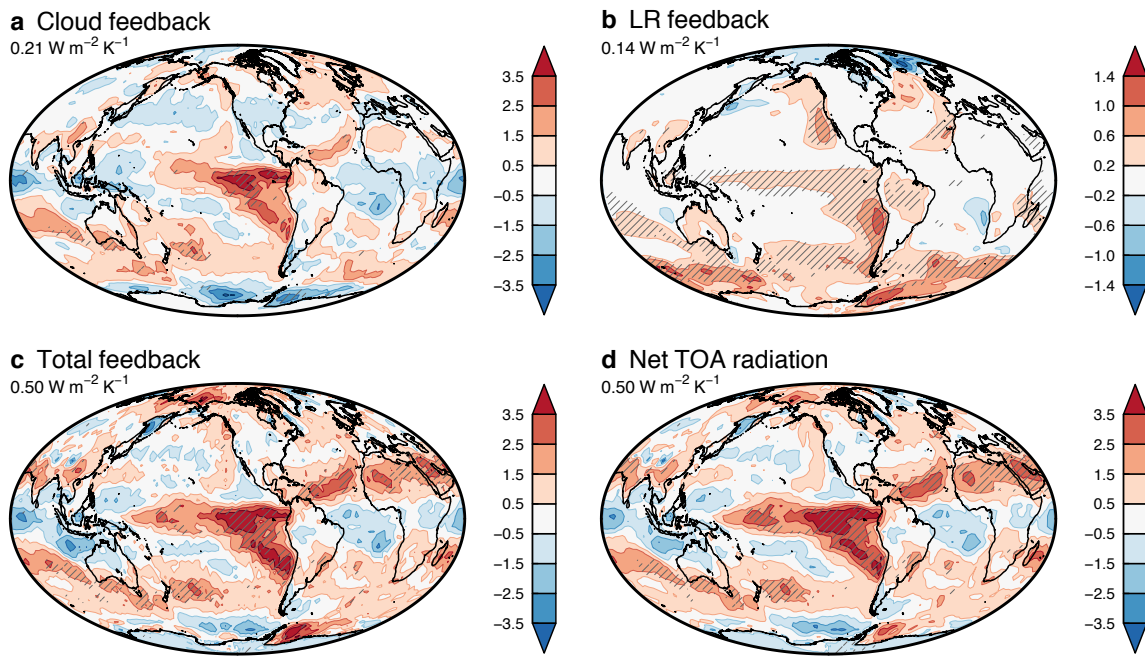
**Fig. 2.** Global-mean feedback parameter, calculated by the Gregory method (1), decomposed into contributions from uniform vertical warming (Planck feedback), non-uniform vertical warming (lapse rate), and changes in relative humidity, surface albedo, and clouds. The cloud term is further broken down into shortwave and longwave changes. “Total” refers to the sum of the feedbacks; the residual is the difference between the sum of the kernel-derived feedbacks and the actual feedback based on net top-of-atmosphere radiation (Materials and Methods). Shown are (a) the feedbacks calculated separately for the early (years 1–20) and late (21–150) periods, and (b) the difference taken as late minus early period. Blue, red and gray circles denote individual models (Table S1), while black circles are mean values.

southern latitudes. Comparing panels (c) and (d) in Fig. 3 confirms that the feedback decomposition accurately captures the actual evolution of changes in top-of-atmosphere net radiation, so that the spatial feedback patterns are not artifacts of the methodology.

**Observed relationship between tropospheric stability and radiative budget.** We have shown the existence of a relationship between SST pattern, tropospheric stability, and the radiative budget in climate models. Can a similar link be observed in the real world to confirm the realism of the modeled responses? Reliable satellite observations of the Earth’s radiative budget are too short to allow for meaningful trend calculations. However, the proposed relationship between long-term changes in stability and radiative balance may also hold in the context of interannual variations. Climate models show qualitatively similar interannual relationships between SST, EIS and the radiative budget in the context of unforced variability to those found at decadal time scales under abrupt CO<sub>2</sub> quadrupling (compare Figs. 1, 3, and S5). In the following, we will demonstrate from observations that real-world year-to-year fluctuations in tropospheric stability are associated with SST and radiative anomalies consistent with the evolution of these variables in climate models.

Figure 4 shows the patterns of SST, EIS, cloud-radiative effect (CRE, defined as all-sky minus clear-sky net down-

373  
374  
375  
376  
377  
378  
379  
380  
381  
382  
383  
384  
385  
386  
387  
388  
389  
390  
391  
392  
393  
394  
395  
396  
397  
398  
399  
400  
401  
402  
403  
404  
405  
406  
407  
408  
409  
410  
411  
412  
413  
414  
415  
416  
417  
418  
419  
420  
421  
422  
423  
424  
425  
426  
427  
428  
429  
430  
431  
432  
433  
434



435  
436  
437  
438  
439  
440  
441  
442  
443  
444  
445  
446  
447  
448  
449  
450  
451  
452  
453  
454  
455  
456  
457  
458  
459  
460  
461  
462  
463  
464  
465  
466  
467  
468  
469  
470  
471  
472  
473  
474  
475  
476  
477  
478  
479  
480  
481  
482  
483  
484  
485  
486  
487  
488  
489  
490  
491  
492  
493  
494  
495  
496

**Fig. 3.** Multi-model mean spatial patterns of changes in climate feedback, calculated as late (years 21–150) minus early (1–20) period. The total feedback in (c) is the sum of the kernel-derived feedbacks (Materials and Methods), while (d) shows the actual feedback based on the regression of net top-of-atmosphere radiation onto global-mean surface temperature. Numbers in the top left corner of each panel denote global-mean values. Hatching denotes a multi-model mean anomaly larger than one standard deviation.

ward top-of-atmosphere radiation), and net downward top-of-atmosphere radiation, all regressed onto annual- and global-mean EIS anomalies, using 16 years of gridded observational and reanalysis data (note that global-mean EIS excludes regions poleward of 50°; Materials and Methods). Since the regression coefficients would represent changes consistent with a 1-K global-mean EIS increase, we multiply the coefficients by the multi-model mean change in the derivative of EIS with respect to global-mean surface temperature ( $-0.16 \text{ K K}^{-1}$ ; Fig. 1b), to obtain observed anomalies comparable in sign and magnitude with the model ensemble. Note that the impact of any changes in global-mean surface temperature has been regressed out (Materials and Methods), to minimize the contribution of the Planck response to the global-mean radiative anomalies. The observed SST pattern associated with an EIS decrease features positive SST anomalies in the tropical and subtropical East Pacific (Fig. 4a). Although no substantial cooling is observed in the warm pool, the anomalous east–west SST gradient across the tropical Pacific is in broad qualitative agreement with the difference between patterns of SST change in climate models (Fig. 1a), causing a decrease in stability in the East Pacific (Fig. 4b).

Consistent with observed relationships between EIS and low cloud, the EIS decrease coincides with a region of positive CRE anomaly, which is reflected in the net top-of-atmosphere radiative change (Fig. 4c–d). The net observed global radiative anomaly ( $0.62 \text{ W m}^{-2} \text{ K}^{-1}$ ) is larger than the multi-model-mean radiative response associated with a  $-0.16 \text{ K K}^{-1}$  EIS change ( $0.50 \text{ W m}^{-2} \text{ K}^{-1}$ ); however, considering the differences in observed SST and EIS patterns relative to the forced climate change signal in models (compare Fig. 1 with Fig. 4a–b), and given the relatively low signal-to-noise ratio in the

short observational record of 16 years, the agreement between observations and models should be interpreted qualitatively, rather than quantitatively. In further support of our findings, similar relationships between tropical SST pattern and low cloud amount have been observed in the context of decadal trends over the 1983–2005 period (15).

CRE anomalies can be affected not only by changes in clouds, but also by non-cloud anomalies in temperature, moisture and surface albedo. By adjusting the CRE anomalies for non-cloud factors (Materials and Methods), we confirm the contribution of clouds to the stability-induced interannual radiative anomalies in observations and models (Figs. S6a, S7a). Decomposing the stability-induced radiative changes into individual components using kernels, we find that lapse rate changes also contribute to the positive radiative anomalies in the East Pacific and in the global mean (Figs. S6b, S7b), but note that the total kernel-derived radiative changes overestimate the actual observed radiative anomalies by about 13% (Fig. S6c–d). Differences between kernel-derived and observed anomalies could be associated with errors in reanalysis temperature and moisture data, inaccuracies in the radiative kernel method (31, 32), or errors in satellite radiances (33). Despite these limitations, our observational analysis does qualitatively support the notion that decreasing tropospheric stability promotes a decrease in radiative cooling to space through changes in clouds and tropospheric lapse rate, consistent with the evolution towards higher effective climate sensitivity in CO<sub>2</sub>-forced climate model experiments.

## Summary and Discussion

Climate models predict that, as the planet warms, the response of tropospheric stability to global warming will gradually be

497  
498  
499  
500  
501  
502  
503  
504  
505  
506  
507  
508  
509  
510  
511  
512  
513  
514  
515  
516  
517  
518  
519  
520  
521  
522  
523  
524  
525  
526  
527  
528  
529  
530  
531  
532  
533  
534  
535  
536  
537  
538  
539  
540  
541  
542  
543  
544  
545  
546  
547  
548  
549  
550  
551  
552  
553  
554  
555  
556  
557  
558

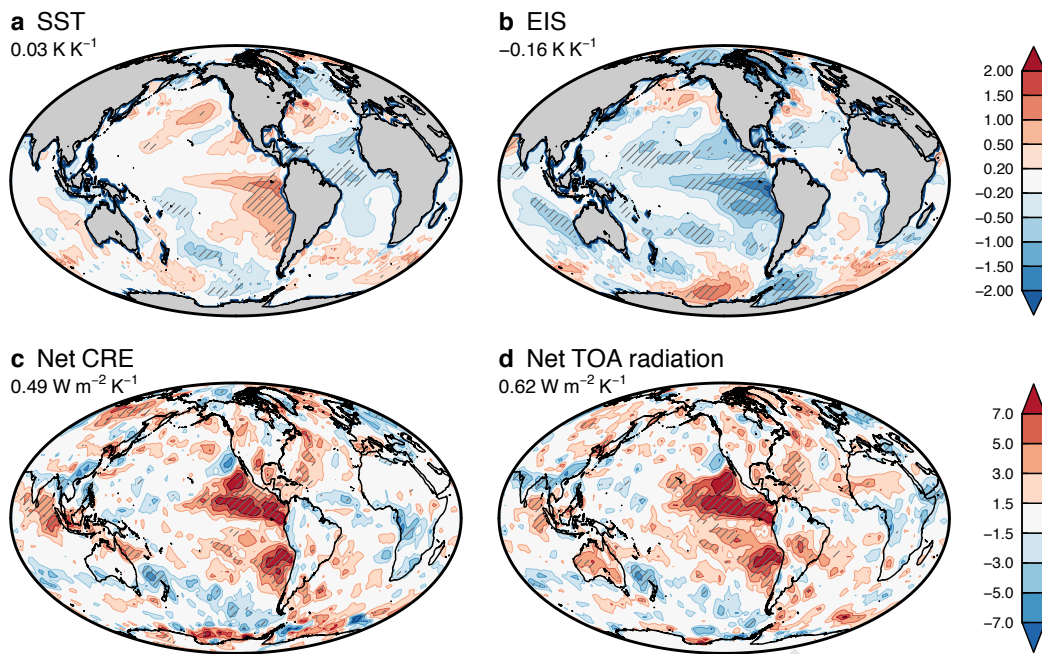


**Fig. 4.** Anomalies of (a) SST, (b) EIS, (c) net CRE, and (d) net top-of-atmosphere radiation regressed onto global- and annual-mean EIS anomalies, for the period December 2000–November 2016 based on global gridded observational and reanalysis datasets (Materials and Methods). The regression coefficients are rescaled by a factor of  $-0.16 \text{ K K}^{-1}$  EIS change, to aid comparison with the results in Figs. 1 and 3. Numbers in the top left corner of each panel denote global-mean values. Hatching indicates a statistically significant regression coefficient at the 5% level.

come more negative, in a manner determined by the evolution of SSTs. The change in stability favors a decrease in low cloud cover (a positive shortwave cloud feedback) and a less negative lapse rate feedback. Although these effects dominate, part of the increase in net feedback (mainly due to changes in surface albedo and humidity) cannot be simply explained by the change in stability; these additional contributions result either from a change in the spatial weighting of local feedbacks (7), or from other unexplained mechanisms. The evolution of climate feedbacks exhibits a spatial structure that closely matches the distribution of stability changes, being most pronounced in the tropical East Pacific, a region characterized by relatively low SST, stable conditions, and extensive marine low cloud. We further show that qualitatively similar relationships between SST pattern, tropospheric stability, and the radiative budget are found in observations on interannual time scales. Therefore, to the extent that future patterns of SST change resemble those of past variability, observational evidence is consistent with the evolution towards a higher effective climate sensitivity during the transient response to CO<sub>2</sub> forcing in climate models.

Further work is needed to fully understand the implications of SST anomaly patterns for tropospheric stability and the Earth's radiative budget. In particular, the relative importance of anomalous zonal SST gradients within the tropics versus anomalous meridional gradients between tropics and extratropics remains unknown. While our results suggest a crucial role for zonal gradients within the tropical Pacific, previous work has suggested that anomalous meridional SST gradients (or relatedly, anomalies in the meridional gradient of ocean heat uptake) could have large impacts on climate

feedbacks (18–20). Further model experiments with idealized (18, 19) and realistic (14, 15, 19, 34) SST anomaly patterns will provide additional insight into the relationships between global anomalies in SST, stability, and the radiative budget.

## Materials and Methods

**Model data.** The evolution of SST, EIS, and climate feedbacks is analyzed in Coupled Model Intercomparison Project phase 5 (CMIP5) climate model output during the 150 years following abrupt quadrupling of atmospheric CO<sub>2</sub> concentrations starting from pre-industrial conditions (the “abrupt4xCO<sub>2</sub>” experiment). We analyze monthly-mean values of temperature, specific humidity, surface albedo, and upward and downward radiative fluxes at the top of atmosphere (TOA) for both all- and clear-sky conditions. The 25 models with available data are listed in Table S1. To remove any potential model drift, anomalies are calculated by subtracting the pre-industrial (pi-Control) integration from the corresponding parallel abrupt4xCO<sub>2</sub> integration. Only the first ensemble member is used for each model.

**Feedback analysis.** The contributions of temperature, moisture, surface albedo, and clouds to changes in TOA radiation are diagnosed separately for each month of the abrupt4xCO<sub>2</sub> integration using radiative kernels (31, 32). Kernels are partial derivatives of the TOA radiative flux relative to temperature, water vapor mixing ratio, and surface albedo at each model grid point. Multiplying the kernels by the changes in each of these variables provides an estimate of their contributions to TOA flux changes. Water vapor changes are partitioned into changes consistent with constant relative humidity (included in the temperature feedbacks), and changes in relative humidity (35). The kernels are also used to adjust cloud-radiative effect (CRE) anomalies for changes in non-cloud effects to obtain an estimate of the radiative changes due to clouds only (31). In this study we use kernels calculated with the Community Atmospheric Model version 5 (36).

559  
560  
561  
562  
563  
564  
565  
566  
567  
568  
569  
570  
571  
572  
573  
574  
575  
576  
577  
578  
579  
580  
581  
582  
583  
584  
585  
586  
587  
588  
589  
590  
591  
592  
593  
594  
595  
596  
597  
598  
599  
600  
601  
602  
603  
604  
605  
606  
607  
608  
609  
610  
611  
612  
613  
614  
615  
616  
617  
618  
619  
620

621 The kernel-derived contributions to TOA flux anomalies are  
 622 aggregated into annual-mean values for each model, and converted  
 623 to feedbacks by regressing the radiative flux time series onto global-  
 624 mean surface air temperature (1, 37). Ordinary least-squares  
 625 regressions are calculated separately for years 1–20 and 21–150 of the  
 626 abrupt4xCO<sub>2</sub> experiment (9). We verify the accuracy of the kernel-  
 627 derived feedbacks by a clear-sky linearity test (32, 37), whereby we  
 628 compare the kernel-based sum of clear-sky TOA feedbacks with the  
 629 actual clear-sky feedback obtained by regressing clear-sky net TOA  
 630 radiation onto global-mean surface temperature. In our results we  
 631 only include the 15 models for which the error in kernel-based clear-  
 632 sky feedback is less than 15% of the actual value in both regression  
 633 periods (bolded model names in Table S1; 37). (Since CRE anom-  
 634 alies are based on model output, testing the kernel decomposition  
 635 with clear-sky feedbacks ensures that only kernel-derived quantities  
 636 are used in the test (32).) The results of the feedback analysis  
 637 remain qualitatively unchanged if we include models with clear-sky  
 638 errors larger than 15% in the calculations (Table S1), or if we use an  
 639 alternative set of radiative kernels (31). The feedback residuals are  
 640 computed as actual minus sum of kernel-derived feedbacks (where  
 641 the actual feedback is the regression slope of net TOA radiation  
 642 against global-mean temperature). ECS values (Fig. S2b) are cal-  
 643 culated as the  $x$ -intercepts of the least-squares fits over years 1–20  
 644 and 21–150.

645 **Effect of EIS variations.** The impact of year-to-year variations in tropo-  
 646 spheric stability on the radiative budget is assessed by regression  
 647 analysis in observations and pre-industrial model integrations (using  
 648 50 years of data for each model). As a simple measure of large-scale  
 649 stability changes, we use global-mean EIS, but excluding grid points

648 1. Gregory JM, et al. (2004) A new method for diagnosing radiative forcing and climate sensitiv-  
 649 ity. *Geophysical Research Letters* 31(3):L03205.  
 650 2. Murphy JM (1995) Transient Response of the Hadley Centre Coupled Ocean-Atmosphere  
 651 Model to Increasing Carbon Dioxide. Part I: Control Climate and Flux Adjustment. *Journal of*  
 652 *Climate* 8(1):36–56.  
 653 3. Williams KD, Ingram WJ, Gregory JM (2008) Time Variation of Effective Climate Sensitivity in  
 654 GCMs. *Journal of Climate* 21(19):5076–5090.  
 655 4. Senior CA, Mitchell JFB (2000) The time-dependence of climate sensitivity. *Geophysical*  
 656 *Research Letters* 27(17):2685–2688.  
 657 5. Winton M, Takahashi K, Held IM (2010) Importance of Ocean Heat Uptake Efficacy to Trans-  
 658 ient Climate Change. *Journal of Climate* 23(9):2333–2344.  
 659 6. Andrews T, Gregory JM, Webb MJ, Taylor KE (2012) Forcing, feedbacks and climate sensi-  
 660 tivity in CMIP5 coupled atmosphere-ocean climate models. *Geophysical Research Letters*  
 661 39(9):L09712.  
 662 7. Armour KC, Bitz CM, Roe GH (2013) Time-Varying Climate Sensitivity from Regional Feed-  
 663 backs. *Journal of Climate* 26(13):4518–4534.  
 664 8. Meraner K, Mauritsen T, Voigt A (2013) Robust increase in equilibrium climate sensitivity  
 665 under global warming. *Geophysical Research Letters* 40(22):5944–5948.  
 666 9. Andrews T, Gregory JM, Webb MJ (2015) The Dependence of Radiative Forcing and Feed-  
 667 back on Evolving Patterns of Surface Temperature Change in Climate Models. *Journal of*  
 668 *Climate* 28(4):1630–1648.  
 669 10. Paynter D, Frölicher TL (2015) Sensitivity of radiative forcing, ocean heat uptake, and climate  
 670 feedback to changes in anthropogenic greenhouse gases and aerosols. *Journal of Geophys-  
 671 ical Research: Atmospheres* 120(19):9837–9854.  
 672 11. Knutti R, Rugenstein MAA (2015) Feedbacks, climate sensitivity and the limits of linear mod-  
 673 els. *Philosophical transactions. Series A, Mathematical, physical, and engineering sciences*  
 674 373(2054):20150146.  
 675 12. Armour KC (2017) Energy budget constraints on climate sensitivity in light of inconstant cli-  
 676 mate feedbacks. *Nature Climate Change*.  
 677 13. Proistosescu C, Huybers PJ (2017) Slow climate mode reconciles historical and model-based  
 678 estimates of climate sensitivity. *Science Advances* 3(7).  
 679 14. Gregory JM, Andrews T (2016) Variation in climate sensitivity and feedback parameters dur-  
 680 ing the historical period. *Geophysical Research Letters* 43(8):3911–3920.  
 681 15. Zhou C, Zelinka MD, Klein SA (2016) Impact of decadal cloud variations on the Earth's energy  
 682 budget. *Nature Geoscience* 9(12):871–874.  
 16. Zhou C, Zelinka MD, Klein SA (2017) Analyzing the dependence of global cloud feedback on  
 the spatial pattern of sea surface temperature change with a Green's function approach.  
*Journal of Advances in Modeling Earth Systems*.  
 17. Andrews T, Webb MJ (2017) The dependence of global cloud and lapse-rate feedbacks on  
 the spatial structure of tropical Pacific warming. *Journal of Climate* pp. JCL1–D–17–0087.1.  
 18. Rose BEJ, Armour KC, Battisti DS, Feldl N, Koll DDB (2014) The dependence of transient  
 climate sensitivity and radiative feedbacks on the spatial pattern of ocean heat uptake. *Geo-  
 physical Research Letters* 41(3):1071–1078.  
 19. Rugenstein MAA, Caldeira K, Knutti R (2016) Dependence of global radiative feedbacks on  
 evolving patterns of surface heat fluxes. *Geophysical Research Letters* 43(18):9877–9885.  
 20. Haugstad AD, Armour KC, Battisti DS, Rose BEJ (2017) Relative roles of surface temperature

683 poleward of 50°; including those grid points tends to emphasize  
 684 high-latitude changes at the sea ice margins in climate models, likely  
 685 related to sea ice variability. Since global-mean surface temperature  
 686 anomalies associated with EIS variability will not generally be zero,  
 687 a component of the associated radiative changes will be due to a  
 688 Planck response that is not a direct result of the stability-driven  
 689 cloud and lapse rate responses. Therefore, the fields are jointly  
 690 regressed onto annual global-mean temperature and EIS anomalies  
 691 to isolate the EIS effect, and we present results for the regression  
 692 slopes associated with EIS only.

693 **Observations.** We use Clouds and the Earth's Radiant Energy Sys-  
 694 tem (CERES) monthly gridded global satellite observations of all-  
 695 and clear-sky TOA radiative fluxes during December 2000 – Novem-  
 696 ber 2016. Prior to analysis the values are detrended at each grid  
 697 point by removing a linear trend estimated by least-squares re-  
 698 gression. To estimate the relationship between SST, EIS, and the  
 699 observed radiative budget, we use ERA-Interim (38) reanalysis fields  
 700 of surface and atmospheric temperature, with which we compute  
 701 annual detrended SST and EIS anomalies. In addition to reanalysis  
 702 temperature, we also use moisture and surface albedo reanalysis  
 703 values in combination with radiative kernels to decompose the TOA  
 704 radiative flux anomalies, and to adjust the CRE anomalies for  
 705 non-cloud effects.

706 **ACKNOWLEDGMENTS.** We thank Steve Klein, an anonymous  
 707 reviewer, and the Editor for helpful comments. PC was supported  
 708 by the European Research Council grant “ACRCC” (grant number  
 709 339390); JMG was supported by the NCAS-Climate program.

710 and climate forcing patterns in the inconstancy of radiative feedbacks. *Geophysical Research*  
 711 *Letters* 44.  
 712 21. Held IM, et al. (2010) Probing the Fast and Slow Components of Global Warming by Return-  
 713 ing Abruptly to Preindustrial Forcing. *Journal of Climate* 23(9):2418–2427.  
 714 22. Xie SP, et al. (2010) Global Warming Pattern Formation: Sea Surface Temperature and Rain-  
 715 fall. *Journal of Climate* 23(4):966–986.  
 716 23. Armour KC, Marshall J, Scott JR, Donohoe A, Newsom ER (2016) Southern Ocean warming  
 717 delayed by circumpolar upwelling and equatorward transport. *Nature Geoscience* 9(7):549–  
 718 554.  
 719 24. Long SM, Xie SP, Zheng XT, Liu Q (2014) Fast and Slow Responses to Global Warming: Sea  
 720 Surface Temperature and Precipitation Patterns. *Journal of Climate* 27(1):285–299.  
 721 25. Wood R, Bretherton CS (2006) On the Relationship between Stratiform Low Cloud Cover and  
 722 Lower-Tropospheric Stability. *Journal of Climate* 19(24):6425–6432.  
 723 26. Sobel AH, Held IM, Bretherton CS (2002) The ENSO Signal in Tropical Tropospheric Temper-  
 724 ature. *Journal of Climate* 15(18):2702–2706.  
 725 27. Flannaghan TJ, et al. (2014) Tropical temperature trends in Atmospheric General Circulation  
 726 Model simulations and the impact of uncertainties in observed SSTs. *Journal of Geophysical*  
 727 *Research: Atmospheres* 119(23):13,327–13,337.  
 728 28. Qu X, Hall A, Klein SA, Caldwell PM (2015) The strength of the tropical inversion and its  
 729 response to climate change in 18 CMIP5 models. *Climate Dynamics* 45(1-2):375–396.  
 730 29. Qu X, Hall A, Klein SA, DeAngelis AM (2015) Positive tropical marine low-cloud cover feed-  
 731 back inferred from cloud-controlling factors. *Geophysical Research Letters* 42(18):7767–  
 732 7775.  
 733 30. Myers TA, Norris JR (2016) Reducing the uncertainty in subtropical cloud feedback. *Geo-  
 734 physical Research Letters* 43(5):2144–2148.  
 735 31. Soden BJ, et al. (2008) Quantifying Climate Feedbacks Using Radiative Kernels. *Journal of*  
 736 *Climate* 21(14):3504–3520.  
 737 32. Shell KM, Kiehl JT, Shields CA (2008) Using the Radiative Kernel Technique to Calculate Cli-  
 738 mate Feedbacks in NCAR's Community Atmospheric Model. *Journal of Climate* 21(10):2269–  
 739 2282.  
 740 33. Loeb NG, et al. (2009) Toward Optimal Closure of the Earth's Top-of-Atmosphere Radiation  
 741 Budget. *Journal of Climate* 22(3):748–766.  
 742 34. Webb MJ, et al. (2017) The Cloud Feedback Model Intercomparison Project (CFMIP) contribu-  
 743 tion to CMIP6. *Geoscientific Model Development* 10(1):359–384.  
 744 35. Held IM, Shell KM (2012) Using Relative Humidity as a State Variable in Climate Feedback  
 745 Analysis. *Journal of Climate* 25(8):2578–2582.  
 746 36. Pendergrass AG, Conley A, Vitt F (2017) Surface and top-of-atmosphere radiative feedback  
 747 kernels for CESM-CAM5. *Earth System Science Data Discussions* pp. 1–14.  
 748 37. Caldwell PM, Zelinka MD, Taylor KE, Marvel K (2016) Quantifying the Sources of Intermodel  
 749 Spread in Equilibrium Climate Sensitivity. *Journal of Climate* 29(2):513–524.  
 750 38. Dee DP, et al. (2011) The ERA-Interim reanalysis: configuration and performance of the data  
 751 assimilation system. *Quarterly Journal of the Royal Meteorological Society* 137(656):553–  
 752 597.  
 753 39. Gordon ND, Klein SA (2014) Low-cloud optical depth feedback in climate models. *Journal of*  
 754 *Geophysical Research: Atmospheres* 119(10):6052–6065.



# Supporting information for “Relationship of tropospheric stability to climate sensitivity and Earth’s observed radiation budget”

Ceppi et al. 10.1073/pnas.XXXXXXXXXX

## Supporting Information (SI)

**Text S1: Change in global feedback versus change in global EIS response.** In our calculation of the relationships between the changes in cloud feedback and the changes in global EIS response per unit warming, one model, MIROC-ESM, clearly stands out as an outlier (red circles in Fig. S3). This model features both the most positive change in EIS response, and the most positive change in shortwave and net cloud feedback. In a previous analysis of the relationships between shortwave cloud-radiative effect and meteorology in tropical subsidence regions, MIROC-ESM was the only CMIP5 model to simulate a substantial *positive* relationship between shortwave cloud-radiative effect and EIS (30, their Figs. 2b and S1), consistent with Fig. S3d and contrary to observational evidence.

We have therefore excluded MIROC-ESM from the calculation of the slopes and correlation coefficients in Fig. S3. Including MIROC-ESM would result in a much weaker correlation coefficient between change in cloud feedback and change in EIS response ( $r = [-0.34, -0.18]$  for the shortwave and net components, respectively).

Finally, note that the *positive* relationship between longwave cloud feedback changes and changes in EIS response (Fig. S3e) is not inconsistent with our reasoning, considering that shortwave and longwave cloud feedbacks are generally anticorrelated. The shortwave impact of stability changes dominates the spread in net cloud feedback (Fig. S3f), consistent with our understanding that the inter-model spread in cloud feedbacks is mainly associated with low clouds.

### Text S2: Inter-model spread in climate feedback changes.

The relationships in Fig. S3 suggest that inter-model differences in the evolution of tropospheric stability (as quantified by EIS) contribute to differences in the evolution of the climate feedbacks. However, the substantial scatter in Fig. S3 indicates that global-mean stability changes cannot fully account for the inter-model spread in feedback changes. Here, we briefly discuss other possible contributions to the spread in feedback changes.

First, the sensitivity of climate feedbacks to stability changes is expected to vary from model to model. This applies particularly to cloud feedbacks, since the sensitivity of low clouds to stability changes varies considerably among CMIP5 models (e.g., 30, their Fig. 1). Hence, even if the cloud feedback changes were driven entirely by changes in tropospheric stability in all climate models, we would not obtain a perfect linear relationship in Fig. S3.

Second, processes unrelated to stability must contribute to the evolution of climate feedbacks. For example, the spread in albedo feedback changes is large in our set of models (Fig. 2b) and it is unrelated to the global-mean EIS change index used in Fig. S3 ( $r = -0.02$ ). The evolution of albedo feedbacks is likely related to the evolution of the local SST response per

degree global warming in different models, as suggested by Fig. S4. Cloud responses are controlled by a variety of environmental factors other than stability (e.g., 29). Furthermore, as discussed in the main text, the mechanisms of the evolution of the relative humidity feedback remain unknown; the spread in relative humidity feedback change is only marginally related to the EIS index considered here ( $r = -0.27$ ).

### Text S3: Climate feedbacks based on the local feedback perspective.

One hypothesis for the evolution of the feedback parameter is based on the idea that the spatial pattern of warming determines the relative contributions of local feedbacks to the global-mean radiative budget; consequently, a change in the spatial warming pattern will cause a change in the global feedback parameter if the local feedbacks vary in space (7). In this perspective, the increasing global-mean feedback in global warming simulations as time passes results from the evolution of the surface warming pattern towards enhanced warming in regions of relatively positive local feedbacks. In this section, we demonstrate that this perspective cannot adequately explain the time evolution of the global feedback parameter seen in CMIP5 experiments.

In the local feedback perspective, climate feedbacks are assumed to be constant in time, but spatially varying (i.e. they depend on geographical location  $x$ ). The effective global-mean feedback  $\lambda_{\text{eff}}$  can then be understood as a spatial average of local feedbacks  $\lambda(x)$  weighted by the local contributions to global-mean warming:

$$\lambda_{\text{eff}}(t) = \overline{\lambda(x)P(x, t)}, \quad [1]$$

where  $P(x, t)$  is the normalized warming pattern (defined as local surface warming per unit global warming) and overbars denote spatial averages. Under the assumption of time-independent local feedbacks, any temporal variations in the effective global-mean feedback parameter must arise from variations in  $P(x, t)$ .

We first derive the local feedbacks  $\lambda(x)$ . Since they are assumed constant, we may calculate them using any part of the experiment; we compute them by taking the mean of the last 20 years of the abrupt4xCO2 integrations, minus the mean of the first 10 years. This ensures that rapid adjustments are excluded from the calculation, while maximizing the warming-induced signal. We divide the time-mean kernel-derived radiative anomalies at each point (for each of the components shown in Fig. S4) by the time-mean local surface temperature anomaly. This procedure yields better results than regressing the local radiative anomalies against local warming, because the low signal-to-noise ratio in local radiative anomalies means that the regression slopes are noisy and not robust. Note that for some models, the surface temperature response may be near zero in some regions, resulting in large, unphysical local feedback values when dividing the radiative anomalies by the

125 temperature anomalies. However, we have verified that these  
126 unphysical values have relatively little impact on the global-  
127 mean feedback values, and similar results are obtained if these  
128 grid points are excluded from our calculations.

129 Effective global-mean feedbacks are then calculated for  
130 years 1–20 and 21–150 following Eq. 1. The warming patterns  
131  $P(x, t)$  are calculated by regressing local surface air tempera-  
132 ture onto global-mean surface air temperature over each of the  
133 two periods. As shown in Fig. S4, the total effective global feed-  
134 back derived assuming constant local feedbacks only weakly  
135 increases in time ( $0.05 \text{ W m}^{-2} \text{ K}^{-1}$  in the multi-model mean).  
136 This means that a change in spatial weighting of constant local  
137 feedbacks can only play a secondary role for the evolution of  
138 the relationship between global-mean radiative imbalance and  
139 global-mean temperature; this evolution must result primarily  
140 from changes in the local feedbacks, rather than from changes  
141 in the spatial pattern of warming.

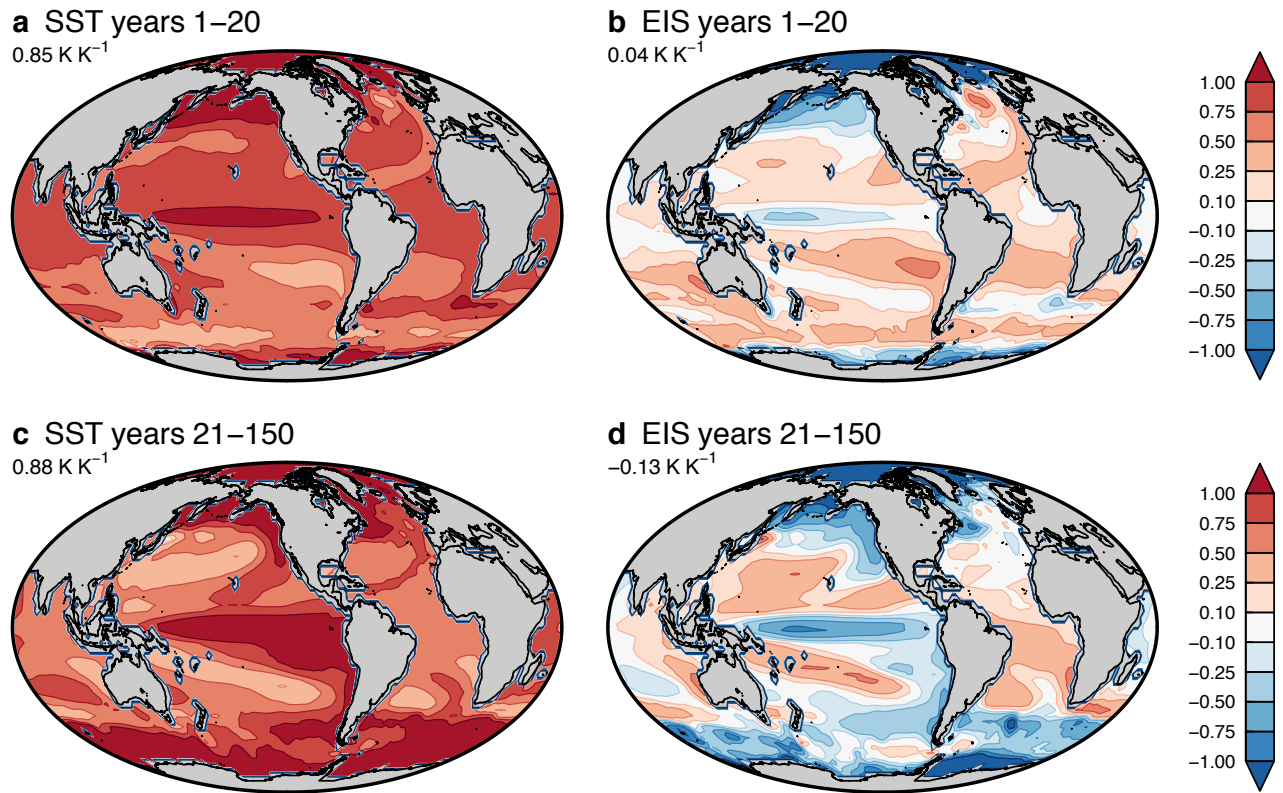
142 The results do suggest, however, that a linear dependence  
143  
144  
145  
146  
147  
148  
149  
150  
151  
152  
153  
154  
155  
156  
157  
158  
159  
160  
161  
162  
163  
164  
165  
166  
167  
168  
169  
170  
171  
172  
173  
174  
175  
176  
177  
178  
179  
180  
181  
182  
183  
184  
185  
186

of feedback processes on local temperature may partly explain 187  
the evolution of the surface albedo feedback ( $0.05 \text{ W m}^{-2}$  188  
 $\text{K}^{-1}$ ). This is unsurprising, since the warming pattern evolves 189  
towards enhanced high-latitude warming over time (Fig. 1; 7). 190  
We have not investigated the mechanism for the weak increase 191  
in relative humidity feedback obtained assuming constant local 192  
feedbacks ( $0.04 \text{ W m}^{-2} \text{ K}^{-1}$ ). We also note that changes in 193  
the spatial weighting of local feedbacks may account for a 194  
substantial fraction of the increase in global feedbacks in a 195  
few of the models (Fig. S4b). 196  
197

Note that even though Fig. S4 indicates that the hypoth- 198  
esis of constant local feedbacks cannot capture the increase 199  
in global cloud feedback over time, it may still explain the 200  
evolution of cloud feedback in some regions, where the cloud 201  
feedback processes are mainly controlled by local temperature 202  
rather than by remote factors – for example phase change 203  
feedbacks in high-latitude regions (39). 204  
205  
206  
207  
208  
209  
210  
211  
212  
213  
214  
215  
216  
217  
218  
219  
220  
221  
222  
223  
224  
225  
226  
227  
228  
229  
230  
231  
232  
233  
234  
235  
236  
237  
238  
239  
240  
241  
242  
243  
244  
245  
246  
247  
248

Model name	Planck	Lapse rate	RH	Albedo	Cloud	LW cloud	SW cloud	Total	Residual
ACCESS1.0	-1.84 (-1.85)	-0.26 (-0.01)	-0.01 (-0.01)	0.37 (0.59)	0.41 (0.48)	0.63 (0.31)	-0.22 (0.17)	-1.33 (-0.80)	0.25 (0.23)
<b>ACCESS1.3</b>	-1.85 (-1.85)	-0.18 (-0.03)	-0.10 (-0.02)	0.50 (0.54)	0.37 (0.78)	0.27 (0.16)	0.10 (0.62)	-1.27 (-0.59)	0.10 (0.10)
<b>BCC-CSM1.1</b>	-1.87 (-1.87)	-0.12 (0.11)	-0.07 (-0.06)	0.41 (0.64)	0.20 (0.28)	0.54 (0.36)	-0.34 (-0.08)	-1.44 (-0.89)	0.09 (0.03)
<b>BCC-CSM1.1(m)</b>	-1.86 (-1.87)	-0.14 (0.06)	-0.12 (-0.07)	0.45 (0.55)	0.27 (0.45)	0.27 (0.45)	-0.00 (-0.00)	-1.40 (-0.88)	0.03 (0.01)
BNU-ESM	-1.87 (-1.85)	-0.04 (0.03)	0.01 (0.07)	0.64 (0.65)	0.17 (-0.08)	0.47 (0.36)	-0.31 (-0.44)	-1.08 (-1.19)	0.12 (0.06)
<b>CanESM2</b>	-1.86 (-1.85)	-0.22 (-0.07)	0.03 (-0.00)	0.38 (0.46)	0.52 (0.49)	0.90 (0.69)	-0.38 (-0.20)	-1.15 (-0.98)	-0.05 (0.08)
<b>CCSM4</b>	-1.85 (-1.87)	-0.12 (0.12)	-0.04 (-0.01)	0.51 (0.64)	-0.02 (0.28)	0.44 (0.28)	-0.46 (0.01)	-1.51 (-0.84)	-0.05 (-0.07)
CNRM-CM5	-1.86 (-1.85)	0.00 (-0.12)	-0.01 (-0.10)	0.67 (0.42)	0.13 (0.17)	0.40 (0.27)	-0.27 (-0.09)	-1.08 (-1.47)	0.03 (0.24)
FGOALS-s2	-1.87 (-1.87)	-0.10 (-0.06)	0.06 (0.06)	0.50 (0.69)	0.02 (0.03)	0.34 (0.53)	-0.32 (-0.50)	-1.39 (-1.15)	0.48 (0.41)
<b>GFDL-CM3</b>	-1.84 (-1.85)	-0.30 (-0.12)	-0.15 (-0.13)	0.44 (0.45)	0.73 (0.96)	0.45 (0.27)	0.28 (0.69)	-1.12 (-0.69)	-0.01 (0.09)
GFDL-ESM2G	-1.84 (-1.84)	-0.34 (-0.07)	0.08 (0.02)	0.25 (0.47)	-0.09 (0.60)	0.92 (0.34)	-1.01 (0.26)	-1.93 (-0.83)	0.36 (0.10)
GFDL-ESM2M	-1.83 (-1.83)	-0.33 (-0.12)	0.01 (0.02)	0.38 (0.40)	0.07 (0.28)	0.88 (0.26)	-0.80 (0.03)	-1.70 (-1.25)	0.34 (0.12)
<b>GISS-E2-H</b>	-1.85 (-1.85)	-0.18 (0.02)	0.11 (0.19)	0.40 (0.38)	-0.22 (-0.07)	0.66 (0.62)	-0.88 (-0.69)	-1.74 (-1.33)	-0.16 (-0.14)
GISS-E2-R	-1.84 (-1.86)	-0.35 (0.04)	0.15 (0.26)	0.32 (0.33)	-0.43 (0.05)	0.80 (0.63)	-1.23 (-0.58)	-2.14 (-1.19)	-0.24 (-0.14)
HadGEM2-ES	-1.85 (-1.85)	-0.14 (-0.04)	-0.00 (0.03)	0.47 (0.52)	0.34 (0.81)	0.59 (0.41)	-0.24 (0.40)	-1.18 (-0.52)	0.37 (0.18)
<b>INMCM4</b>	-1.87 (-1.84)	-0.05 (-0.13)	-0.05 (0.18)	0.53 (0.29)	-0.05 (0.42)	0.27 (0.49)	-0.32 (-0.07)	-1.49 (-1.07)	-0.17 (-0.15)
<b>IPSL-CM5A-LR</b>	-1.84 (-1.84)	-0.28 (-0.23)	-0.04 (0.00)	0.33 (0.35)	1.08 (1.22)	0.51 (0.58)	0.57 (0.64)	-0.76 (-0.50)	-0.11 (-0.08)
<b>IPSL-CM5B-LR</b>	-1.85 (-1.85)	-0.12 (-0.04)	-0.03 (0.03)	0.40 (0.36)	0.39 (0.74)	0.16 (0.48)	0.24 (0.26)	-1.20 (-0.76)	-0.00 (-0.03)
MIROC-ESM	-1.85 (-1.84)	-0.20 (-0.31)	-0.05 (-0.15)	0.71 (0.40)	0.28 (1.19)	0.65 (0.24)	-0.37 (0.96)	-1.10 (-0.70)	0.04 (0.06)
MIROC5	-1.86 (-1.83)	-0.21 (-0.17)	-0.07 (-0.00)	0.47 (0.59)	-0.08 (0.08)	0.26 (0.48)	-0.34 (-0.40)	-1.76 (-1.34)	0.03 (0.14)
<b>MPI-ESM-LR</b>	-1.85 (-1.84)	-0.27 (-0.18)	-0.15 (-0.07)	0.41 (0.58)	0.43 (0.54)	0.57 (0.70)	-0.14 (-0.16)	-1.43 (-0.98)	0.10 (0.07)
<b>MPI-ESM-MR</b>	-1.85 (-1.85)	-0.24 (-0.12)	-0.14 (-0.06)	0.41 (0.65)	0.33 (0.53)	0.48 (0.61)	-0.15 (-0.08)	-1.49 (-0.85)	0.09 (0.03)
<b>MPI-ESM-P</b>	-1.85 (-1.85)	-0.35 (-0.14)	-0.12 (-0.07)	0.27 (0.57)	0.43 (0.48)	0.63 (0.65)	-0.20 (-0.17)	-1.62 (-1.00)	0.12 (0.08)
<b>MRI-CGCM3</b>	-1.86 (-1.84)	-0.17 (-0.06)	-0.10 (-0.06)	0.37 (0.52)	0.28 (0.36)	0.02 (-0.06)	0.26 (0.42)	-1.48 (-1.07)	-0.06 (0.01)
<b>NorESM1-M</b>	-1.86 (-1.87)	-0.14 (0.07)	-0.00 (0.03)	0.40 (0.61)	-0.05 (0.35)	0.32 (0.28)	-0.37 (0.06)	-1.66 (-0.81)	0.02 (-0.02)
Mean (15 models)	-1.85 (-1.85)	-0.19 (-0.05)	-0.06 (-0.01)	0.41 (0.51)	0.31 (0.52)	0.43 (0.44)	-0.12 (0.08)	-1.38 (-0.88)	-0.00 (0.00)
Mean (all models)	-1.85 (-1.85)	-0.19 (-0.06)	-0.03 (0.00)	0.44 (0.51)	0.22 (0.46)	0.50 (0.41)	-0.28 (0.04)	-1.42 (-0.95)	0.07 (0.06)

373  
374  
375  
376  
377  
378  
379  
380  
381  
382  
383  
384  
385  
386  
387  
388  
389  
390  
391  
392  
393  
394  
395  
396  
397  
398  
399  
400  
401  
402  
403  
404  
405  
406  
407  
408  
409  
410  
411  
412  
413  
414  
415  
416  
417  
418  
419  
420  
421  
422  
423  
424  
425  
426  
427  
428  
429  
430  
431  
432  
433  
434



435  
436  
437  
438  
439  
440  
441  
442  
443  
444  
445  
446  
447  
448  
449  
450  
451  
452  
453  
454  
455  
456  
457  
458  
459  
460  
461  
462  
463  
464  
465  
466  
467  
468  
469  
470  
471  
472  
473  
474  
475  
476  
477  
478  
479  
480  
481  
482  
483  
484  
485  
486  
487  
488  
489  
490  
491  
492  
493  
494  
495  
496

**Fig. S1.** Multi-model mean normalized changes in SST and EIS during years 1–20 (a,b) and 21–150 (c,d), calculated by regressing annual-mean SST and EIS against global-mean temperature during the respective periods. Numbers in the top left corner of each panel denote global-mean values.

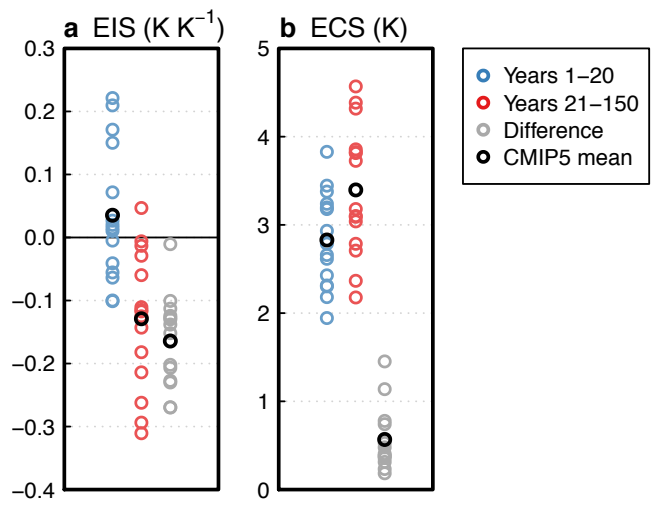


**Fig. S2.** Changes in annual-mean global-mean EIS (a) and ECS (b) during years 1–20 (blue), years 21–150 (red), and the difference between the two periods (gray). Each colored circle represents a model, and black circles denote multi-model means. EIS changes are calculated by regressing global-mean EIS onto global-mean temperature during each period. See the Materials and Methods section for the ECS calculation.

497  
498  
499  
500  
501  
502  
503  
504  
505  
506  
507  
508  
509  
510  
511  
512  
513  
514  
515  
516  
517  
518  
519  
520  
521  
522  
523  
524  
525  
526  
527  
528  
529  
530  
531  
532  
533  
534  
535  
536  
537  
538  
539  
540  
541  
542  
543  
544  
545  
546  
547  
548  
549  
550  
551  
552  
553  
554  
555  
556  
557  
558

559  
560  
561  
562  
563  
564  
565  
566  
567  
568  
569  
570  
571  
572  
573  
574  
575  
576  
577  
578  
579  
580  
581  
582  
583  
584  
585  
586  
587  
588  
589  
590  
591  
592  
593  
594  
595  
596  
597  
598  
599  
600  
601  
602  
603  
604  
605  
606  
607  
608  
609  
610  
611  
612  
613  
614  
615  
616  
617  
618  
619  
620

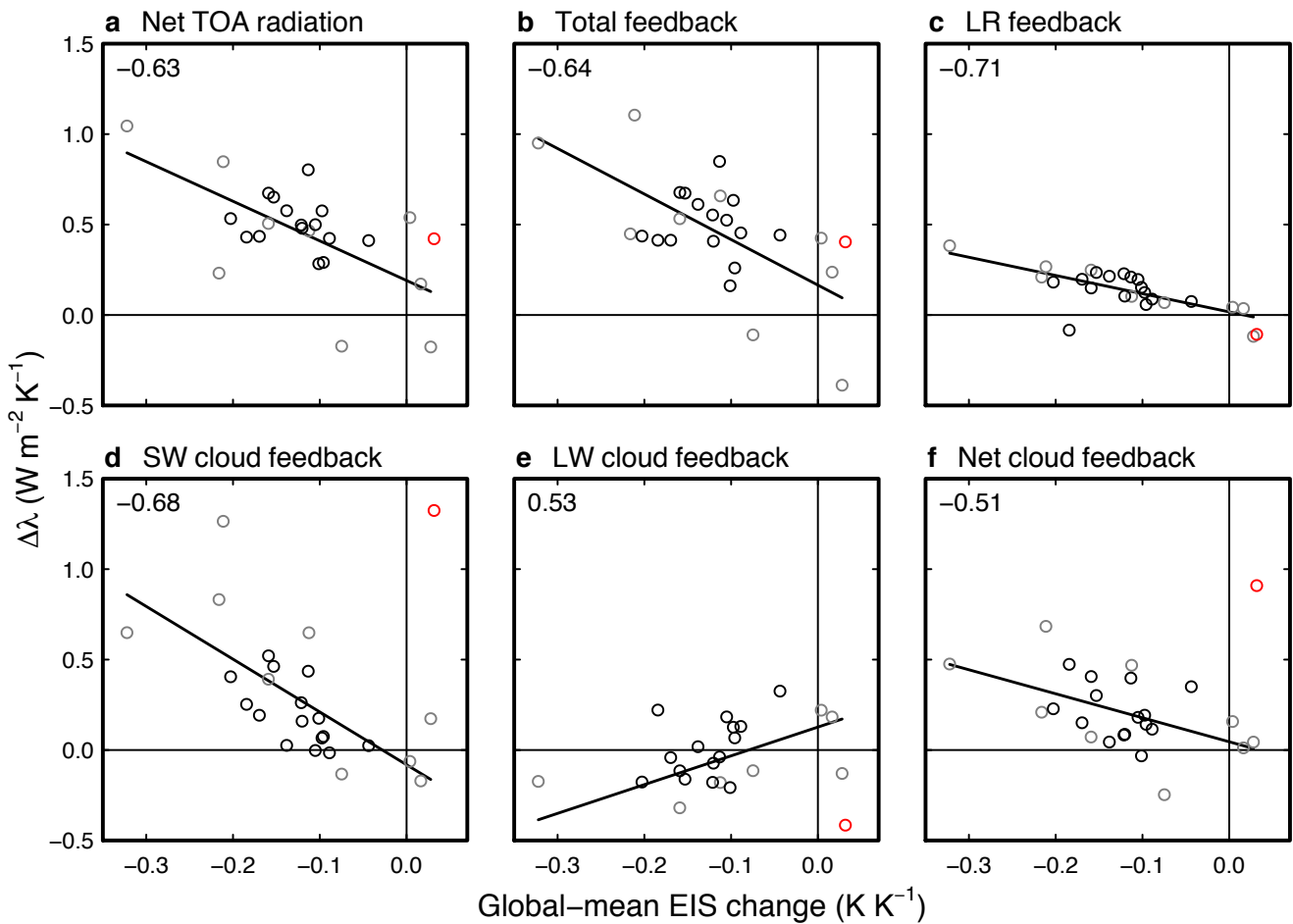


**Fig. S3.** Change in feedback parameter versus change in global-mean EIS response per unit warming. Shown are changes in (a) net feedback based on TOA radiation, (b) the sum of kernel-derived feedbacks, (c) lapse rate feedback, (d)–(f) shortwave, longwave, and net cloud feedback. The changes are calculated as late (years 21–150) minus early (1–20) period. Black lines denote ordinary least-squares regression slopes. Black circles denote the 15 models used in the analysis; the red circle represents an outlier model, MIROC-ESM, excluded from the calculation of the regression slopes and correlation coefficients (Text S1); and gray circles represent the remaining 9 models (Table S1). The correlation coefficients are calculated for all models, minus MIROC-ESM. Note that regions poleward of 50° are excluded from the global-mean EIS calculation (Materials and Methods).

621  
622  
623  
624  
625  
626  
627  
628  
629  
630  
631  
632  
633  
634  
635  
636  
637  
638  
639  
640  
641  
642  
643  
644  
645  
646  
647  
648  
649  
650  
651  
652  
653  
654  
655  
656  
657  
658  
659  
660  
661  
662  
663  
664  
665  
666  
667  
668  
669  
670  
671  
672  
673  
674  
675  
676  
677  
678  
679  
680  
681  
682

683  
684  
685  
686  
687  
688  
689  
690  
691  
692  
693  
694  
695  
696  
697  
698  
699  
700  
701  
702  
703  
704  
705  
706  
707  
708  
709  
710  
711  
712  
713  
714  
715  
716  
717  
718  
719  
720  
721  
722  
723  
724  
725  
726  
727  
728  
729  
730  
731  
732  
733  
734  
735  
736  
737  
738  
739  
740  
741  
742  
743  
744

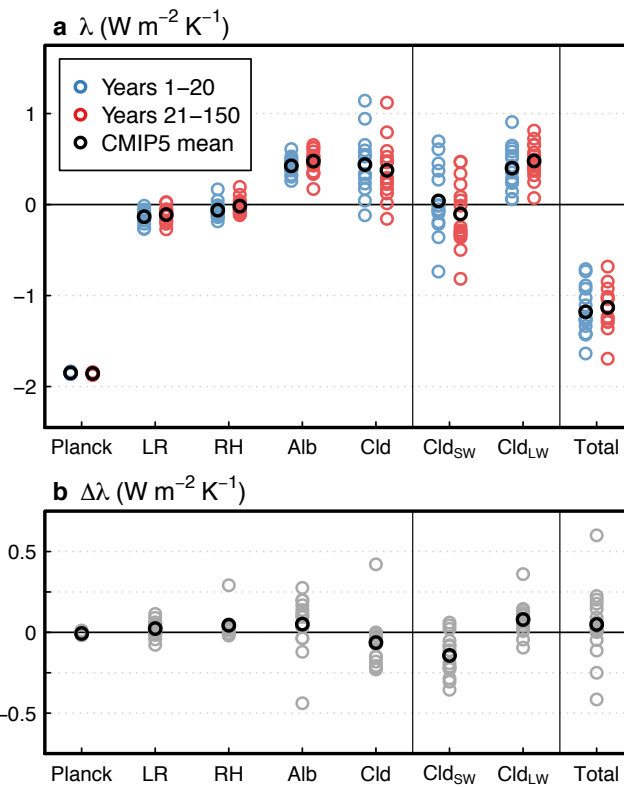


**Fig. S4.** As in Fig. 2 but showing feedback values calculated following the local feedback perspective of Armour et al. (7). See Text S3 for details of the calculation method.

745  
746  
747  
748  
749  
750  
751  
752  
753  
754  
755  
756  
757  
758  
759  
760  
761  
762  
763  
764  
765  
766  
767  
768  
769  
770  
771  
772  
773  
774  
775  
776  
777  
778  
779  
780  
781  
782  
783  
784  
785  
786  
787  
788  
789  
790  
791  
792  
793  
794  
795  
796  
797  
798  
799  
800  
801  
802  
803  
804  
805  
806

807  
808  
809  
810  
811  
812  
813  
814  
815  
816  
817  
818  
819  
820  
821  
822  
823  
824  
825  
826  
827  
828  
829  
830  
831  
832  
833  
834  
835  
836  
837  
838  
839  
840  
841  
842  
843  
844  
845  
846  
847  
848  
849  
850  
851  
852  
853  
854  
855  
856  
857  
858  
859  
860  
861  
862  
863  
864  
865  
866  
867  
868

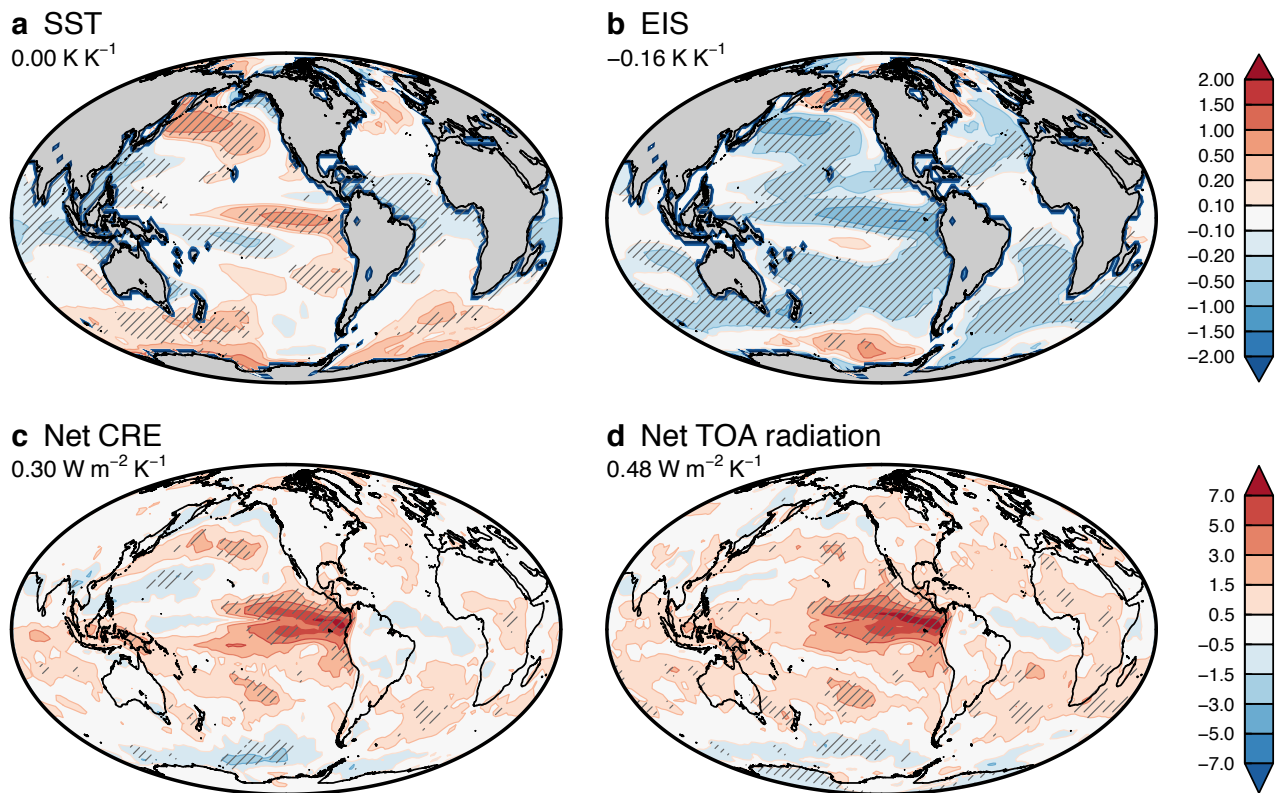


**Fig. S5.** As in Fig. 4, but using pre-industrial control data in the 15 models used in the analysis. Shown are the multi-model mean regression patterns, rescaled to yield anomalies consistent with a  $-0.16 \text{ K K}^{-1}$  global-mean EIS change to aid comparison with Figs. 1 and 3. Hatching denotes a multi-model mean anomaly larger than one standard deviation. Note that the effect of changes in global-mean surface temperature has been regressed out (Materials and Methods).

869  
870  
871  
872  
873  
874  
875  
876  
877  
878  
879  
880  
881  
882  
883  
884  
885  
886  
887  
888  
889  
890  
891  
892  
893  
894  
895  
896  
897  
898  
899  
900  
901  
902  
903  
904  
905  
906  
907  
908  
909  
910  
911  
912  
913  
914  
915  
916  
917  
918  
919  
920  
921  
922  
923  
924  
925  
926  
927  
928  
929  
930

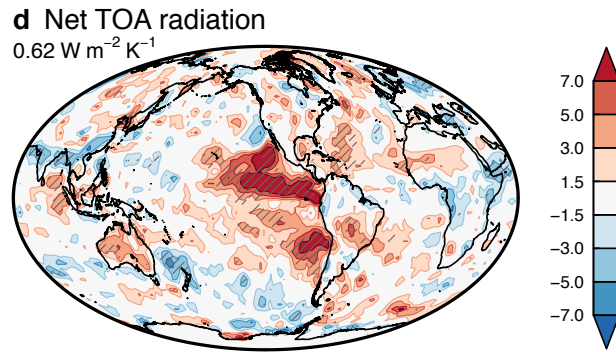
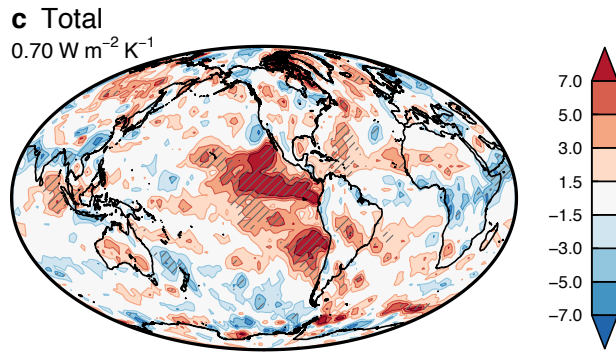
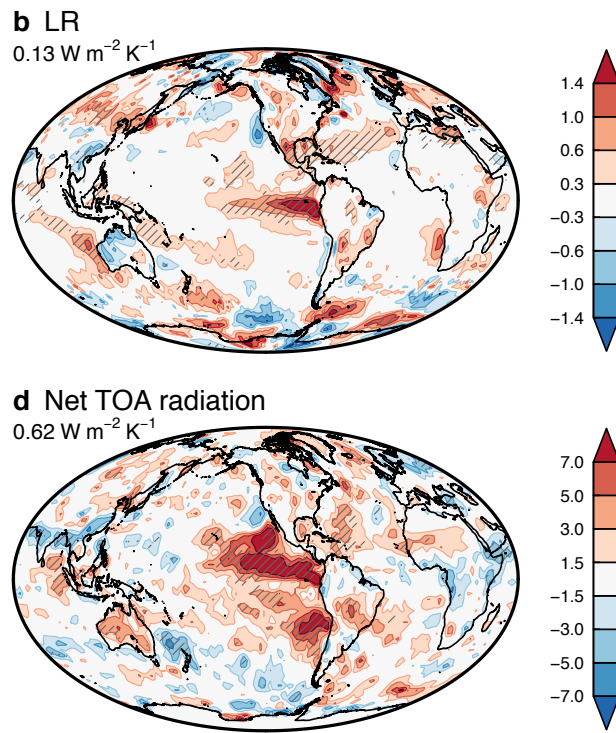
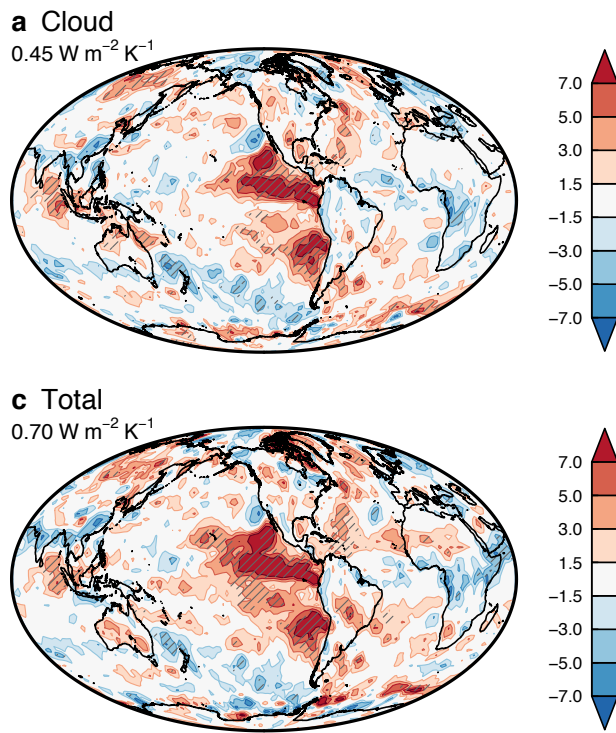


**Fig. S6.** Contributions to stability-induced top-of-atmosphere radiative anomalies in observations by (a) clouds, (b) lapse rate changes, and (c) the sum of all the components (Planck, lapse rate, water vapor, surface albedo, and clouds). Panel (d) shows the actual net radiative anomalies (as in Fig. 4d) for comparison with (c). The radiative anomaly decomposition in (a)–(c) was calculated with radiative kernels (Materials and Methods). All the anomalies are scaled for a  $-0.16 \text{ K K}^{-1}$  change in global-mean EIS for comparison with climate model results (cf. main text and Fig. 4). Hatching indicates a statistically significant regression coefficient at the 5% level.

931  
932  
933  
934  
935  
936  
937  
938  
939  
940  
941  
942  
943  
944  
945  
946  
947  
948  
949  
950  
951  
952  
953  
954  
955  
956  
957  
958  
959  
960  
961  
962  
963  
964  
965  
966  
967  
968  
969  
970  
971  
972  
973  
974  
975  
976  
977  
978  
979  
980  
981  
982  
983  
984  
985  
986  
987  
988  
989  
990  
991  
992

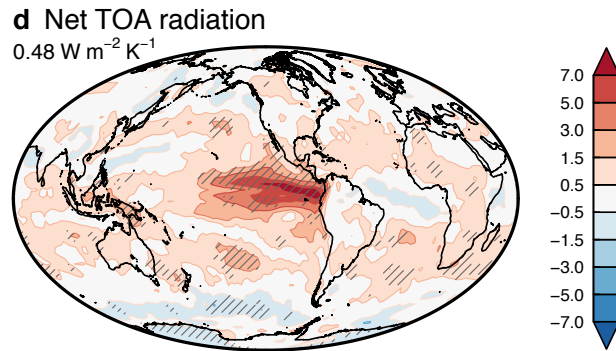
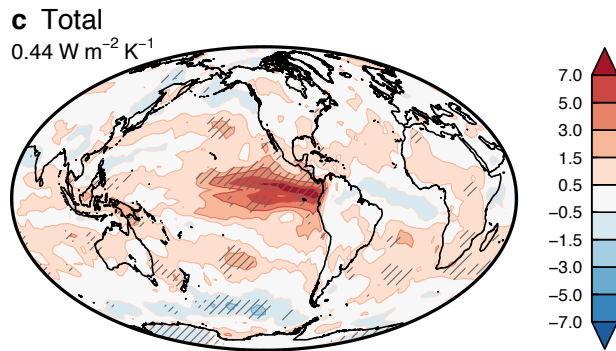
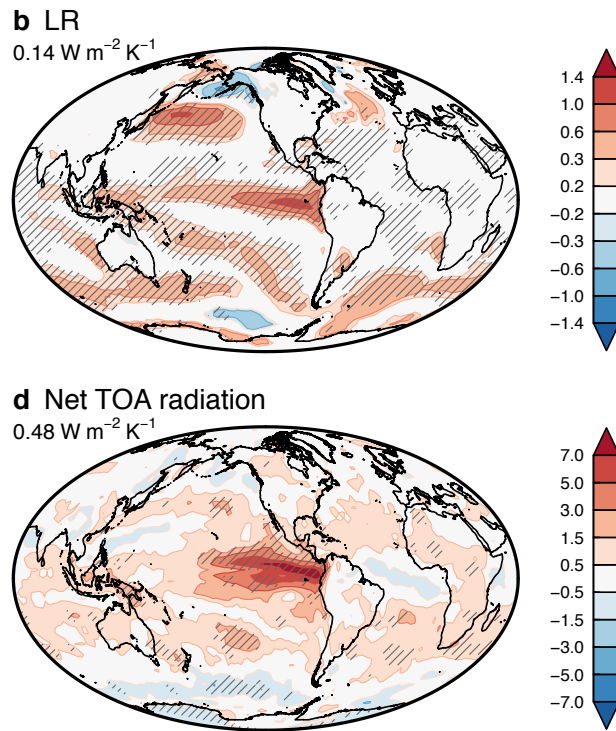
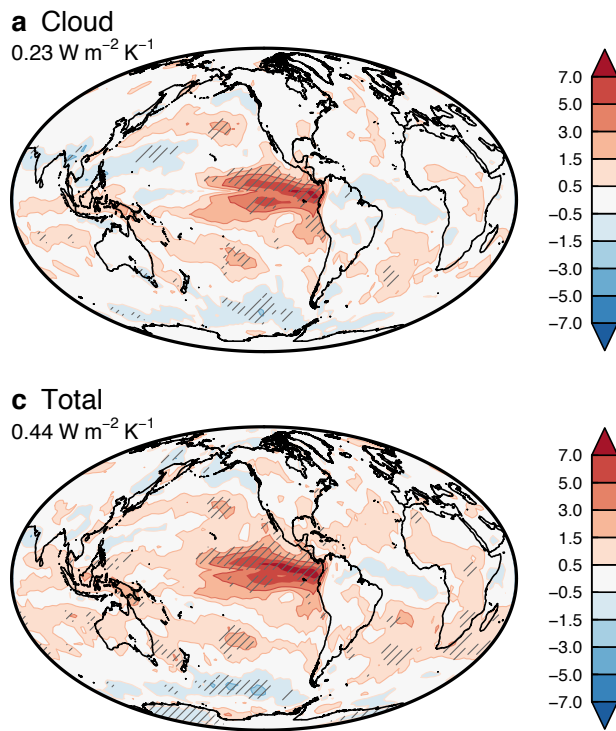


**Fig. S7.** As in Fig. S6, but for the interannual stability-induced radiative anomalies in climate models (cf. Fig. S5). Shading represents multi-model mean results, and hatching denotes a multi-model mean anomaly larger than one standard deviation across models.